

Linköping Studies in Science and Technology

Licentiate Thesis No. 1540

# High pressure and high temperature behavior of TiAlN

Niklas Norrby



**Linköping University**

LIU-TEK-LIC-2012:25

NANOSTRUCTURED MATERIALS

DEPARTMENT OF PHYSICS, CHEMISTRY AND BIOLOGY (IFM)

LINKÖPING UNIVERSITY

SWEDEN

©Niklas Norrby

ISBN: 978-91-7519-863-7

ISSN: 0280-7971

Printed by LiU-Tryck, Linköping, Sweden, 2012

---

## ***Abstract***

---

This licentiate thesis mainly reports about the behavior of arc evaporated TiAlN at high pressures and high temperatures. The extreme conditions have been obtained in metal cutting, multi anvil presses or diamond anvil cells. Several characterization techniques have been used, including x-ray diffraction and transmission electron microscopy.

Results obtained during metal cutting show that the coatings are subjected to a peak normal stress in the GPa region and temperatures around 900 °C. The samples after metal cutting are shown to have a stronger tendency towards the favorable spinodal decomposition compared to heat treatments at comparable temperatures. We have also shown an increased anisotropy of the spinodally decomposed domains which scales with Al composition and results in different microstructure evolutions. Furthermore, multi anvil press and diamond anvil cell at even higher pressures and temperatures (up to 23 GPa and 2200 °C) also show that the unwanted transformation of cubic AlN into hexagonal AlN is suppressed with an increased pressure and/or temperature.



---

## *Preface*

---

This is a summary of my work between April 2010 and April 2012. During these years, the main focus of my work has been to study the behavior of arc evaporated TiAlN at high pressures and high temperatures with the key results presented in the appended papers. The work has been performed in the group Nanostructured Materials at the Department of Physics, Chemistry and Biology (IFM) at Linköping University. High pressure experiments have also been performed at the Bayerisches Geoinstitut in Bayreuth. It has been supported by Seco Tools AB and the SSF project Designed multicomponent coatings, Multifilms.



---

## ***Aim of the work***

---

The aim of this thesis is to explore the behavior of TiAlN at both high temperatures and high pressures. One of the reasons for this is the use of TiAlN as a protective hard coating on metal cutting inserts. Hence, the successful characterization of coatings used in metal cutting is important. During a typical cutting operation, temperatures up to around 900 °C and normal stresses up to several GPa occur at the tool-chip-interface. The work in the thesis mainly focuses on the effect of the stress or pressure on the decomposition and connects it to metal cutting operations.



---

## ***Included papers***

---

### **Paper I**

*Pressure and temperature effects on the decomposition of arc evaporated  $Ti_{0.6}Al_{0.4}N$  coatings during metal cutting*

**N. Norrby**, M. P. Johansson, R. M'Saoubi and M. Odén

Submitted for publication

### **Paper II**

*High pressure and high temperature behavior of  $Ti_{0.6}Al_{0.4}N$*

**N. Norrby**, H. Lind, M. P. Johansson, F. Tasnádi, N. Dubrovinskaia, L.S. Dubrovinsky, I.A. Abrikosov and M. Odén

In manuscript

### **Paper III**

*Microstructural anisotropy effects on the metal cutting performance of decomposed arc evaporated  $Ti_{1-x}Al_xN$  coatings*

M. P. Johansson, **N. Norrby**, J. Ullbrand, R. M'Saoubi and M. Odén

In manuscript



---

## *Acknowledgements*

---

Magnus Odén, my supervisor

Mats Johansson, my co-supervisor

Rachid M'Saoubi, for valuable contributions to my papers

My colleagues in the Nanostructured Materials, Thin Film and Plasma groups

My colleagues in the Theoretical Physics group, especially Igor, Ferenc and Hans for successful collaboration

Everyone at Seco Tools AB for being so friendly and helpful

Bayerisches Geoinstitut in Bayreuth, for giving me a warm welcome every time I visit your beautiful city

Family and friends, especially Camilla



---

## *Table of contents*

---

Introduction	- 1 -
Materials science – an introduction	- 3 -
Thin film deposition	- 9 -
Ti <sub>1-x</sub> Al <sub>x</sub> N	- 13 -
Characterization techniques	- 17 -
High pressure techniques	- 27 -
Metal cutting	- 33 -
Conclusions	- 39 -
References	- 41 -
Summary of included papers	- 45 -
Paper I	- 47 -
Paper II	- 63 -
Paper III	- 81 -



# CHAPTER 1

---

## *Introduction*

---

Most people probably encounter thin films or coatings on a daily basis without thinking of it. The numerous applications include the electrical coatings in a cell phone, anti reflective coatings on glasses and camera lenses or decorative coatings on buildings. The application studied in this work is however protective coatings deposited on metal cutting inserts. The inserts are used in turning and milling operations with a huge variety of end products. The industry's strive for higher cutting speeds drives the research and development into improved tools. The use of a protective coating on a cutting tool can in many cases increase the tool lifetime several times. Since the introduction of protective coatings on metal cutting inserts in the late 1960s [1,2] their market share of cemented carbide inserts has grown to around 90 % [3].

The material system used in this work is the ternary ceramic compound TiAlN which has been used in the industry since the 1980s [4,5]. Its predecessor was TiN and originally Al was added to the system with the intention of improving the poor oxidation behavior of TiN at temperatures exceeding 500 °C [6,7]. Additionally, TiAlN exhibits not only a better oxidation behavior compared to TiN at elevated temperature but also demonstrates an age hardening behavior. Hence, at elevated temperature, the hardness decrease due to defect annihilation is not only avoided but the coating also shows an increased hardness.

Due to the extensive research around TiAlN, its high temperature behavior is well known in the literature [8-11]. During metal cutting

however, the coating is also subjected to a stress distribution in the GPa region along the cutting edge [12,13]. To this point, little is known of how high pressures and high temperatures (HPHT) affect the coating properties, except for a few theoretical studies [14,15]. This thesis is a first step to experimentally explore the HPHT behavior of TiAlN.

# CHAPTER 2

---

## ***Materials science – an introduction***

---

Understanding of macroscopic material properties such as hardness and thermal properties requires information on the atomic level. Important questions include why phase transformations occur and the effect of external parameters such as temperature and pressure. By gaining insight in this, the possibility arises to control and tailor the material to desired properties. In principal, it would be possible to summarize materials science in two words, namely *energy minimization*, as this is what all materials strive for.

### **2.1 Phases and phase transformations**

Many materials are crystalline, i.e. their atoms are arranged in a long range ordered lattice extending in three dimensions. For each periodic lattice, unit cells can be derived for different phases where the most common include the body centered cubic (bcc), face centered cubic (fcc) and hexagonal close packed (hcp). Most of the materials rearrange into different phases when exposed to variations in e.g. temperature and pressure. One example is iron which at room temperature is stable in the bcc structure and then transforms into fcc at temperatures above 900 °C. This is followed by a final transformation into bcc again at temperatures above 1400 °C before melting [16].

The preferred, or stable, phase for a material is governed by thermodynamics, i.e. the stable state is the state with a minimized free energy. An example can be seen in Figure 1 where the system's energy is

lowest at position C, meaning that a system at position A would like to transform into position C. However, as the system is situated at a local minimum at position A it is said to be in a metastable state. A transformation from its metastable to the most energetically favorable state must involve the passing of the energy barrier marked in B. In other words, a material remains in its metastable state unless the energy barrier is passed.

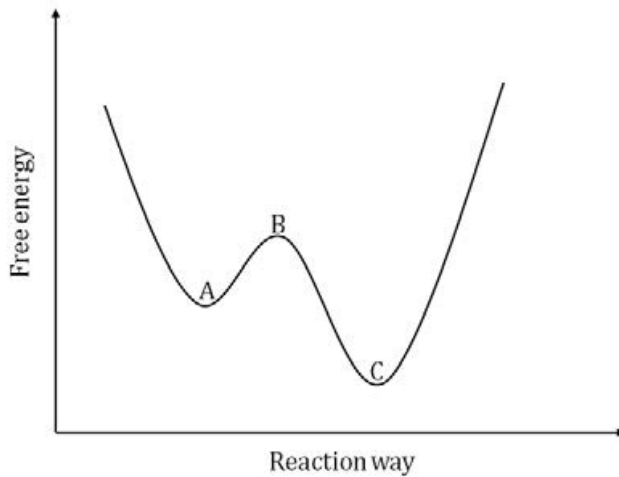


**Figure 1. Schematic free energy along a reaction path. The local minimum at position A indicate a metastable state whereas the minimum at position C shows a stable configuration.**

Another limitation for the system to transform is often that the system's temperature must be elevated enough for diffusion processes to occur, i.e. the kinetics may limit a thermodynamically driven process. Exceptions to this include diffusionless phase transformations, such as the martensitic transformation. When all the prerequisites are met for a transition, it can occur through a number of processes, including *nucleation and growth* and *spinodal decomposition*, both of them described in more detail below. Nucleation and growth requires the above mentioned passing of an energy barrier whereas this is not required during spinodal decomposition.

### 2.1.1 *Nucleation and growth*

If the energy of the system can be lowered by the introduction of a new phase with a composition very different from the matrix, the new phase first has to nucleate before any growth process starts. The nucleation is either homogenous, which takes place in a uniform solution, or heterogeneous where the nucleation begins at grain boundaries or impurities in the solution.

If it is assumed that a homogenous nucleation initiates with a spherical nuclei of a composition different from the matrix, there is an increase in energy roughly proportional to the surface energy. For a small nucleus, this is a dominating energy term over the gain in energy, hence a small compositional fluctuation in the mixture will increase the total energy. Homogenous nucleation therefore usually only occurs after super cooling, i.e. when the gain in energy due to the nucleation is very large. Once the nucleus has started to grow in size, the gain in energy dominates due to the fact that it is proportional to the cubed radius whereas the surface energy is associated to the squared radius. Thus, after the radius of the nucleus has exceeded a critical value, the growth can proceed.

The surface energy is a less contributing factor at heterogeneous growth due the reduced surface of the new nuclei, nucleation is therefore commonly heterogeneous. Still, there is a nucleation barrier to climb and small compositional fluctuations will be restored. As the nuclei grow, regions surrounding them are soaked from atoms, giving rise to ordinary down-hill diffusion from the matrix.

### 2.1.2 *Spinodal decomposition*

It is possible to obtain a solid solution of two immiscible components, e.g. by quenching an alloy with a composition inside the spinodal in Figure 2 from an elevated temperature. Here, the spinodal is defined within the region where the second derivative of the free energy is negative. However, as the free energy of this system is at a local maximum it is highly unstable against compositional fluctuations. Hence, even small deviations in the composition will lower the total energy as opposed to

nucleation and growth. Therefore, there is no nucleation barrier associated with the spinodal decomposition and it may occur spontaneously over a large volume. Solutions inside the spinodal are often referred to as unstable and not metastable due to this instability against fluctuations in the composition. The diffusion process during spinodal decomposition is up-hill diffusion, i.e. atoms move towards regions already enriched of that atom opposite to the diffusion during nucleation and growth.

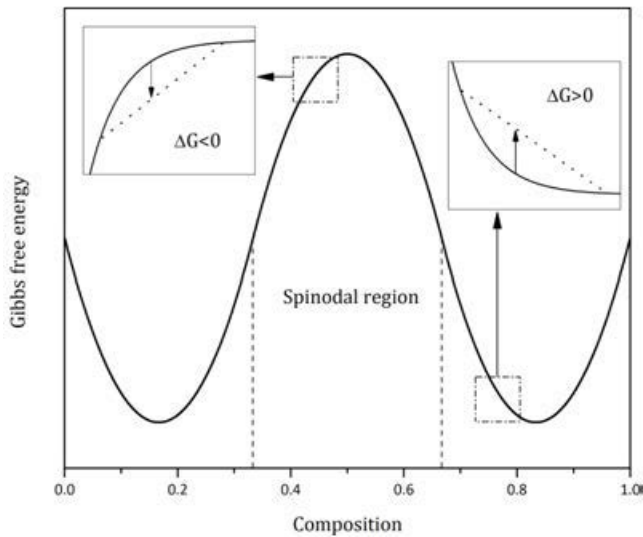


**Figure 2. A free energy curve as a function of composition at a given temperature. The second derivative of the curve determines whether an infinitesimal change in composition lowers or increases the total energy.**

Typical composition profiles during the two processes can be seen in Figure 3 below. Nucleation and growth in Figure 3 (a) gives few sharp interfaces whereas these occurring after spinodal decomposition in Figure 3 (b) are more subtle but over a large volume. What must be considered is though that the composition profiles are valid before the spinodally decomposed domains are coarsened.

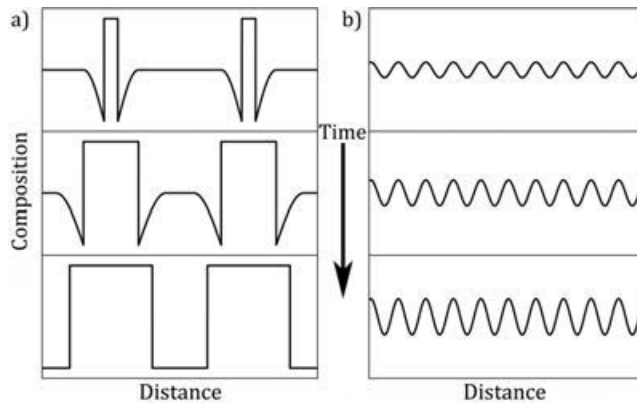


**Figure 3. Schematic composition profiles at different times (increasing time downwards) after a) nucleation and growth and b) spinodal decomposition. After [17].**

## 2.2 Hardening mechanisms

The definition for the hardness of a material is how good the resistance is against plastic deformation [18]. The theoretical hardness of a perfect crystal is however several times higher than what is observed for most materials [19]. The reason for the lower hardness obtained in experiments is that the plastic deformation is drastically assisted by the sliding of linear defects, dislocations, present in the crystal. Hence, the hardness is often increased by introducing different means to obstruct the dislocation movement. This can be achieved with e.g. grain boundary hardening, deformation hardening, solution hardening and precipitation hardening. The most relevant for this work is a form of precipitation hardening through age hardening.

### 2.2.1 Age hardening

If nanometer sized coherent regions with a small lattice mismatch and a deviation of their elastic properties precipitates in the material, coherency strains will be introduced in the lattice. The strain fields interact with the dislocations in a way that an increased energy is required to pass them. A schematic graph over how the dislocations pass the obstacles is shown in Figure 4.

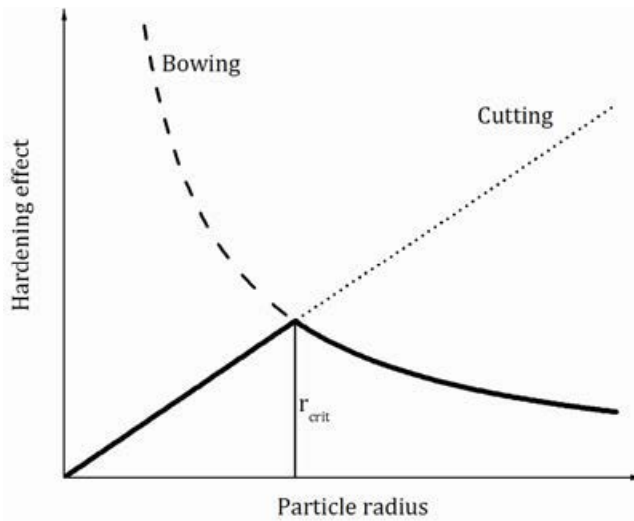


**Figure 4. Hardening effect and dislocation interaction with increasing particle radius. After [20].**

Up to a critical radius ( $r_{crit}$ ) of the precipitates, the dislocations cut through them which give a hardening effect that is linear to the particle radius. If the regions are coarsened, the coherency may be lost by the introduction of misfit dislocation around the precipitate. When this occurs, the dislocations will instead bow around the precipitates, a process known as Orowan hardening [21]. This hardening effect instead decreases with an increased particle radius and is after some point completely lost, a phenomena described as over ageing.

A good example, and relevant for this thesis, is the age hardening effect in TiAlN first observed by Hörling *et al* [8]. The unstable solid solution of TiAlN first decomposes spinodally at elevated temperatures into coherent cubic (c-) TiN and c-AlN (rocksalt, B1 structure) enriched domains, giving rise to an increased hardness due to the mechanisms explained above. With further annealing, a transformation from c-AlN to its thermodynamically stable hexagonal phase (wurtzite, B4 structure), h-AlN, occurs. The transformation is associated with a volume increase and a coherency loss and the hardness is rapidly decreased.

# CHAPTER 3

---

## *Thin film deposition*

---

Most often, there are several paths to choose when depositing a thin film. A first rough division among methods is between chemical vapor deposition (CVD) and physical vapor deposition (PVD) where both methods have their advantages and disadvantages. In this work, a PVD method called reactive cathodic arc evaporation is used to deposit the coatings.

### **3.1 Chemical vapor deposition**

Typically, CVD introduces a gaseous deposition material in a chamber where it chemically reacts to form the coating, either with the substrate itself or with another gas forming a compound to be grown. This gives the possibility to deposit on very complex shapes as the gases can penetrate into variations of substrate cavities.

The chemical reaction however usually forms a large amount of waste gases which have to be considered as they might be harmful to the environment. The problem with waste gases is not current for PVD coatings where the deposition material is condensed directly on the substrate, without the intermediate chemical reaction. On the other hand, the ability to deposit thin films on complex shapes is not as good as with CVD.

## 3.2 Physical vapor deposition

A numerous of different PVD methods exist, where the most common are arc evaporation and sputtering [22]. The basic principle for all PVD techniques can though be divided into three steps. The first step is to synthesize the deposition material which includes a transition from a solid or liquid phase into a vapor phase. In the second step, the vaporized deposition material is transported to the substrate. Finally, in the third step, the deposition material is condensed on the substrate surface followed by nucleation and growth of the thin film.

The largest difference between techniques is often in the first step. In sputtering, highly energetic ions bombard the target which then spits out the deposition material into the plasma whereas the target is locally melted and evaporated by an arc in cathodic arc evaporation [23].

### 3.2.1 *Reactive cathodic arc evaporation*

Reactive cathodic arc evaporation, where reactive stands for the use of a reactive gas, is widely used in the cutting tool industry due to its ability to produce dense and adherent coatings. In the process, a cathode of the desired material is hit by an electrical arc from an electrode which creates a plasma discharge. As a result of the small spot hit by the arc, the current density is locally very high on the cathode surface. This generates a temperature high enough to evaporate neutral atoms, ions and electrons from the cathode surface.

A high degree of ionization is achieved in the ionization zone [24] whereupon the ions are attracted by the negatively biased substrates and transported to the substrate surface. The reactive gas and the ions are finally condensed at the substrate surface and the film is nucleated and grown. The films are in general in a compressive stress state due to the heavy ion bombardment during deposition.

During the arc discharge, so called macro particles are ejected from the cathode as well. These macro particles, also called droplets, consists of molten cathode material and may be detrimental to the positive mechanical properties of the thin film. Solutions to this problem include the use of shields or magnetic filters [25], in common for all

solutions is though a reduced deposition rate which makes them relatively unusual in the cutting tool industry.

The arc evaporation system used in this work is a commercial system used in the industry. The deposition has been executed in nitrogen atmosphere with compound cathodes of Ti and Al. The substrates, made of WC-Co or iron sheets, are positioned on a drum which rotates during deposition around the cathodes. As there are three cathode positions along the height on each side of the chamber there is a possibility to deposit compositionally homogenous coatings using the same cathode composition at all positions. However, if a desired composition is not available as cathode there is also a possibility to mount different cathode compositions along the height. This was used in **Paper I** where a pure Ti cathode was used in combination with a  $\text{Ti}_{0.50}\text{Al}_{0.50}$  cathode mounted in two positions at different height in the chamber. The result was a gradiental composition change along the height of the inserts positioned on the drum whereupon the wanted coating composition could be selected with analytical instruments.



## CHAPTER 4

---

### *Ti<sub>1-x</sub>Al<sub>x</sub>N*

---

One of the first material systems for protective coatings to be deposited on cutting inserts were the ceramic compound TiN. Its crystal structure is the cubic NaCl (c-TiN) structure which is easiest described as an fcc lattice with a two atom (Ti and N) basis with coordinates (0,0,0) and  $(\frac{1}{2}, \frac{1}{2}, \frac{1}{2})$ . The use of TiN coated cutting tool was motivated by their good properties compared to uncoated tools [26]. However, for today's cutting tools industry and their demand for higher cutting speeds yielding increasing cutting temperatures, more advanced materials than TiN are required. The addition of Al in to the material system was therefore made as a first attempt to increase the oxidation behavior. It was though soon discovered that the superior cutting performance of TiAlN compared to TiN could not completely be addressed to the better oxidation resistance, but also to an age hardening effect at elevated temperatures due to the decomposition.

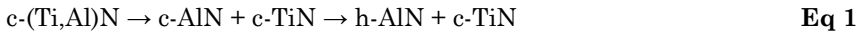
#### **4.1 Decomposition of Ti<sub>1-x</sub>Al<sub>x</sub>N**

The solubility of AlN into TiN is thermodynamically only a few atomic percent at best [27]. The low deposition temperature during cathodic arc evaporation though enables the growth of unstable c-(Ti,Al)N up to an aluminum content around 70 % [28] where the Al atoms are distributed randomly at Ti sites in the lattice. At elevated temperatures, it has been shown that the metastable c-(Ti,Al)N decomposes in two steps. In the

first step, coherent c-TiN- and c-AlN-rich nanostructured cubic domains are formed [11].

Because of the miscibility gap and that *ab initio* calculations [29] show a negative second derivative of Gibb's free energy, this first isostructural decomposition is often regarded as a spinodal type. The coherent domains give rise to an increase in hardness because of an effective hindering of dislocation motion induced by the coherency strain and the difference of elastic properties as is described in section 2.2.1 *Age hardening* above.

At ambient pressures however, the c-AlN is not stable and as the AlN enriched domains grow with time the stable form of AlN, hexagonal structure, is transformed from c-AlN [8]. This second decomposition step is detrimental to coating properties and following it is a rapid decrease in hardness, mainly due to the coherency loss and volume increase of associated with the transformation. To summarize, the decomposition of c-TiAlN can be described as in Eq 1.



## 4.2 Anisotropic effects

It has theoretically been shown by Ferenc *et al* [30] that the alloying of Al into TiN results in a higher elastic anisotropy which has large microstructural effects on the spinodal decomposition [31]. The study shows that at Al contents higher around 0.3 the <100> directions are the elastically softer with an increased tendency with the higher Al content. In **Paper III** it is shown that this elastic anisotropy aligns the spinodally decomposed domains into the <100> directions for  $\text{Ti}_{0.34}\text{Al}_{0.66}$  after both metal cutting and heat treatments. This is however not as clear for  $\text{Ti}_{0.60}\text{Al}_{0.40}$  as this composition is much closer to the isotropic limit around 0.3. These effects during spinodal decomposition are also similar to what is observed by Baker *et al* in another system [32]. This effect is a possible explanation to the better flank wear resistance demonstrated by high Al content coatings as different shapes of the decomposed domains will give a different hardening.

### 4.3 The influence of pressure

There exist two theoretical papers [14,15] which describe and predict the high pressure behavior of TiAlN. Alling *et al* [14] explains the behavior with the fundamental thermodynamic equation in Eq 2 for calculating the Gibb's free energy at a given temperature:

$$\left(\frac{\partial \Delta G}{\partial p}\right)_T = \Delta V \quad \text{Eq 2}$$

where G is the Gibb's energy, V the volume, p the pressure and the presence of the  $\Delta$  is the change according to Eq 3.

$$\Delta M = M_{Ti_{1-x}Al_xN} - (1-x)M_{TiN} - xM_{AlN} \quad \text{Eq 3}$$

$(M = G, V)$

Hence, the change in volume is the deviation from Vegard's behavior which shows a linear dependence of the volume with respect to the composition of the components [33]. This deviation has earlier been shown to be positive for the isostructural case both experimentally [34] and theoretically [35]. For the non-isostructural case on the other hand, the result is the opposite due to the large volume increase originating from the c-AlN to h-AlN transformation.

Consequently, the applied pressure during e.g. a cutting operation as well as the compressive stress state in the as-deposited coatings promotes the spinodal decomposition of TiAlN. The experimental findings of this are the main result of **Paper I** where the spinodal compositional wavelength is measured after both metal cutting and heat treatments. It was shown that the average wavelength was overall increased after metal cutting compared to after heat treatments despite comparable temperatures and times. Hence, it was concluded that the spinodal decomposition is promoted by the applied stresses during metal cutting.

Using first principles calculations, the theoretical phase diagram for AlN in Figure 5 was obtained in **Paper II**. **Figure 5** also shows the experimental values for TiAlN.

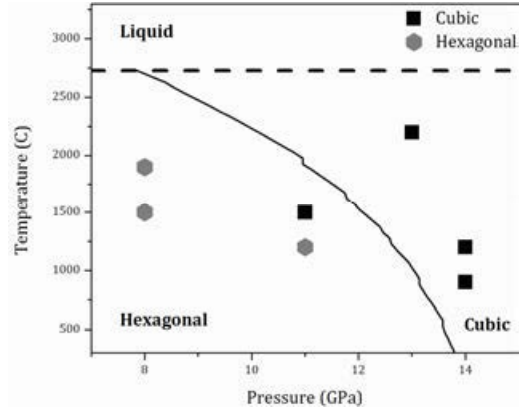


**Figure 5.** Phase diagram showing the stability regions of AlN at different temperatures and pressures. Data points show experimental values obtained for TiAlN.

From the findings, it can be concluded that an increased pressure and/or temperatures also stabilizes the cubic phase of AlN, consistent with previous findings [36-39]. The results though imply that the alloying of Ti into AlN further stabilizes the cubic phase of AlN, possibly through a template effect as nanometer sized regions of c-AlN are surrounded by coherent regions of c-TiN. Also, the increase in elastic energy associated with the c-AlN to h-AlN transformation is likely to further stabilize the cubic phase. To summarize, an external pressure is favorable for the high temperature behavior both by promoting the spinodal decomposition and by suppressing the cubic to hexagonal transformation.

# CHAPTER 5

---

## *Characterization techniques*

---

Characterization techniques include means to study material properties such as structural, chemical, and thermal properties. All these have been studied in this work using a variety of experimental setups.

### **5.1 X-ray diffraction**

X-ray diffraction (XRD) is probably one of the most used characterization instruments in the world of thin films. This is mainly due to its ability to characterize e.g. phases or internal and external stresses in the samples while also being a non-destructive technique. Furthermore, as the sample preparation needed is little or none, XRD is a fast and convenient method. The principle behind XRD is the fact that x-ray wavelengths are in the same order as the atomic distances in materials. The scattering of x-rays by the core electrons gives rise to constructive and destructive interference according to the superposition principle. The conditions for constructive interference are shown by Bragg's law in Eq 4 below.

$$n\lambda = 2d \cdot \sin 2\theta \qquad \text{Eq 4}$$

where  $n$  is an integer,  $\lambda$  the x-ray wavelength,  $d$  the distance between adjacent parallel planes and  $2\theta$  the scattering angle. Bragg's law is though only a first condition for constructive interference to occur since some scattering planes in crystal structures (with a few exceptions such as the simple cubic structure) will interfere destructively despite being

fulfilled by Bragg's law. This can however be solved by combining Bragg's law with the structure factor for the specific crystal structure. By doing this for e.g. an fcc lattice, it can be determined that the only planes that allow constructive interference is those where  $h$ ,  $k$  and  $l$  are either all even or all odd. Hence, diffraction from  $\{100\}$  planes does not occur, whereas scattering from  $\{200\}$  does.

Another method is to first construct the reciprocal lattice vector  $\mathbf{G}$  according to Eq 5 and Eq 6.

$$\mathbf{G} = \sum_1^3 \mathbf{b}_i \cdot n_i \quad n_i = h, k \text{ and } l \quad \text{Eq 5}$$

$$\mathbf{b}_1 = \frac{2\pi(\mathbf{a}_2 \times \mathbf{a}_3)}{|\mathbf{a}_1 \times \mathbf{a}_2 \cdot \mathbf{a}_3|} \quad (\text{cyclic permutation}) \quad \text{Eq 6}$$

where  $\mathbf{b}$  is the reciprocal primitive basis vectors and  $\mathbf{a}$  the real space equivalent. Constructive interference then occurs when  $\mathbf{G}$  is equal to the difference between the scattered wave vector  $\mathbf{k}'$  and incident wave vector  $\mathbf{k}$ . Using this method, the structure factor is not necessary to evaluate since only reflections from allowed  $hkl$  planes are included in the reciprocal lattice.

Several setups of diffractometers are available but the one used in this work was a high brilliance transmitting diffractometer with a two-dimensional detector. The diffraction gives rise to intense rings when a polycrystalline material is examined, as is seen in Figure 6 (a). Here, the radius of the rings is proportional to the scattering angle, hence inversely proportional to the plane distance. Integration of the spectrum gives the line plot in Figure 6 (b) which simplifies interpretation of the data. Ideally, the peaks would have been sharp but this is not the case, instead relatively broad peaks are seen. This is usually due to either small crystal grains or to internal strain which locally shrinks or enlarges the unit cell.

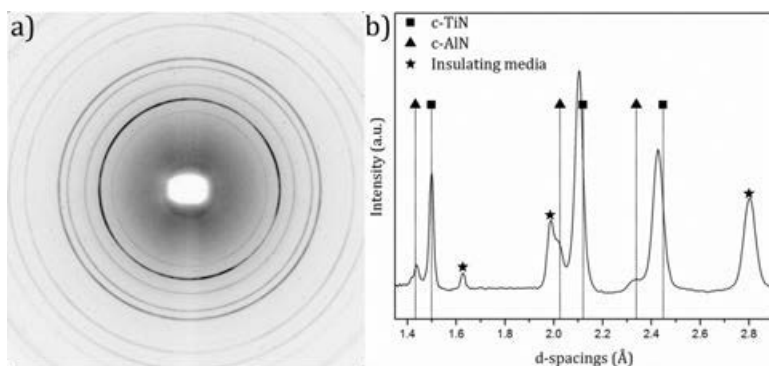


**Figure 6.** Diffractograms from a diamond anvil cell sample shown as a) two dimensional area diffractograms and b) integrated radially into a one dimensional line plot.

## 5.2 Electron Microscopy

Compared to light optical microscopy (LOM), the biggest advantage with an electron microscope (EM) is the improved resolution. The ability to image with electrons originates in the wave-particle duality where all particles can be described as a wave with a de Broglie wavelength. Basically, the resolution is determined by the Rayleigh criterion, where there is a linear dependence between the resolution and the wavelength of the electron or photon. Since the wavelength of visible light is around 500 nm while the relativistic electron wavelength for an acceleration voltage of 100 keV is around 0.004 [40] the resolution is to a great extent improved with electrons. The value of the wavelength does not give the whole picture though, since it is relatively easy to construct good glass lenses for LOM, which is not the case for the electromagnetic lenses used in EM. The development of EM lenses is however progressing, hence lowering the resolution to better values.

### 5.2.1 Scanning Electron Microscopy

In a scanning electron microscope (SEM) an electron probe is scanned on the surface of the sample to be examined. The electron energy is usually varied between a few and several tens of keV. With larger electron energies, the resolution is improved but to the expense of a reduced surface sensitivity due to an increased electrons probe interaction volume. When compared to the transmission electron microscope,

described below, SEM offers a much lower image resolution. However, due to ease of use, simple sample preparation and micrographs which often are easy to interpret and understand, SEM analyses are frequently used in material science.

Electron beam to sample interactions, e.g. secondary electrons, backscattered electrons and x-rays, are frequently used in the SEM for generating image contrast. Secondary electrons are generated from ionization of the sample atoms, hence giving topographic contrast as a result of shadowing effects. The backscattered electrons are elastically scattered primary electrons where the scattering is more dominant for heavier elements, hence a Z-contrast in the micrograph is shown. Finally, the emitted x-rays can be used to determine and distinguish between elements in the sample. This is described in more detail below in *5.2.5 Energy dispersive x-ray spectroscopy*.

### *5.2.2 Transmission Electron Microscopy*

As the name implies, electrons in a transmission electron microscope (TEM) are transmitted through the sample. It uses an acceleration voltage of several hundred keV which gives a better resolution compared to SEM, thus improving the magnification ability.

There are several contrast mechanisms in a TEM, e.g. thickness, diffraction and phase contrast. If the electron passes through a thicker region of the sample it will be more heavily absorbed or scattered, hence thicker regions will appear darker.

By introducing an objective aperture, diffracted electron beams will be blocked which introduces more diffraction contrast in the micrograph. Hence, by tilting the sample it is possible to find grains which diffract strongly, i.e. grains in Bragg condition, since they appear darker in the micrograph. Also, a large defect density will introduce diffraction contrast which is usually seen for as-deposited coatings. This imaging mode, where the central beam in the diffraction pattern is transmitted is called bright field imaging and an example is seen in Figure 7 (a).

In Figure 7 (b), another useful mode is used, namely dark field imaging. Here, the objective aperture is used in the diffraction plane to block the central beam or specifically choose a certain diffraction spot. Hence, only beams diffracted by these planes will reach the imaging screen. In the particular case in Figure 7 (b) the technique is used to show that areas rich in h-AlN in a decomposed TiAlN coating are found in the grain boundaries.

Common for bright and dark field is the use of only one beam selected by the objective aperture (either the central or a diffracted beam). Another contrast mechanism, commonly used for high resolution TEM is phase contrast where more than one beam interferes. As is seen in the HRTEM micrograph with the corresponding fast Fourier transforms (FFT) in Figure 7 (c), HRTEM may provide information about lattice spacing and grain orientation. This particular example shows an enlarged view of the grain boundary in Figure 7 (a,b). With aid of FFTs (not shown) it is possible to determine that the upper grain is oriented with a zone axis, i.e. the direction parallel to the electron beam, of [011] and the lower grain with [112] as zone axis.

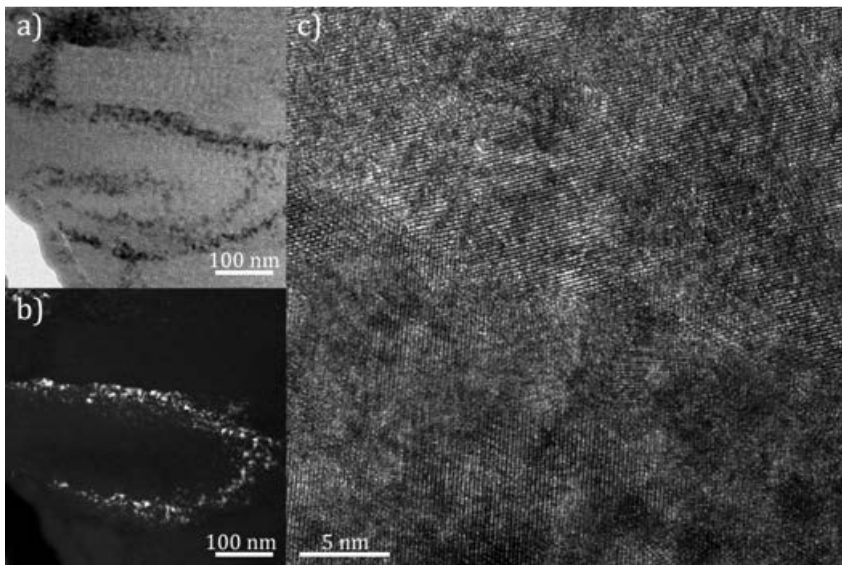


**Figure 7. A TEM sample showing a) bright field, b) dark field and c) high resolution TEM imaging. The sample is TiAlN used in a cutting operation and prepared with focused ion beam.**

### 5.2.3 *Scanning transmission electron microscopy*

The scanning transmission electron microscope (STEM) uses a nanoprobe which is scanned across the specimen, as opposed to the imaging in the TEM mode where a parallel and broad beam is used. The detector used is often a high angle annular dark field (HAADF) detector positioned in the diffraction plane, hence the contrast in a STEM stems from the intensity of all scattered beams in each respective scanning point. Since the scattering is dependent of atomic weight, the two main contrast mechanisms in STEM mode are diffraction contrast and Z-contrast i.e. elemental contrast. Consequently, bright contrast is seen from grains fulfilling the Bragg condition or from heavier elements in the sample. In combination with an energy dispersive x-ray spectroscopy (EDS) detector it is possible to acquire elemental analysis which is valuable when mapping e.g decomposed regions, grain boundaries or the tool-chip interface.

### 5.2.4 *Electron diffraction*

Considering the fact that electrons can behave as waves, constructive and destructive interference occur with electrons similar to x-ray scattering described in section 5.1 *X-ray diffraction*. The main difference is that the electrons are scattered mainly by the nuclei while x-rays are scattered by the core electrons. When performing electron diffraction, the diffraction plane, instead of the image plane, is projected on the fluorescent disc or CCD. In modern TEMs, this task does not require more than pushing a button, making electron diffraction a fast and easy way of determining e.g. texture. Also, by introducing the selected area electron diffraction (SAED) aperture it is possible to obtain a diffraction pattern from a single grain or nano sized feature which is not possible with XRD.

### 5.2.5 *Energy dispersive x-ray spectroscopy*

If the transmitting electrons knock out an electron from the sample atom, a hole is created. When this hole is filled by electrons in higher energy levels, the energy gain is released as an x-ray photon. The photon

energy is characteristic and depends on the element and the involving energy levels. With a detector it is then possible to acquire the spectra, hence determining the contributing elements with their respective fingerprints of characteristic energies. EDS is used either in a SEM or, more importantly for this work, in STEM where the ability to specifically choose a desired region of interest is very valuable.

#### *5.2.6 Conventional TEM sample preparation*

A requirement for TEM samples is that the region of interest is electron transparent. This normally implies a thickness of <100 nm [40] but the thinner the better can be seen as a rule of thumb, especially for HRTEM imaging. To achieve this, the substrates with the thin film on top are cut into appropriate pieces that will fit into a TEM grid. For cross-sectional samples, which is the method used in this work, two pieces are fit with the film side facing each other. The sample is then baked in a mixture of graphite and araldite which is followed by polishing down to a thickness of around 50  $\mu\text{m}$ . The polishing is made with several diamond abrasive cloths with a decreasing size of diamond grains. In the finishing step, an ion miller is used for the final thinning and polishing until electron transparency is achieved.

#### *5.2.7 Focused ion beam*

When working with coatings deposited on cutting inserts used in cutting operations, the focused ion beam (FIB) is a very powerful instrument for obtaining TEM samples. Its ability to specifically choose an area of interest within a few micrometers is extremely useful and essentially not possible with conventional TEM preparation. Basically, the FIB is a SEM with an additional ion column angled from the electron column which can be seen in Figure 8.

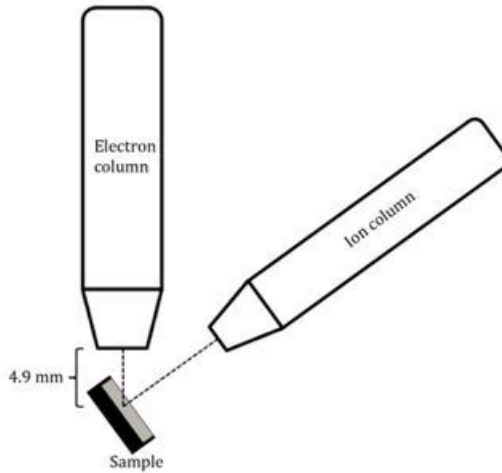


**Figure 8. A schematic picture of a typical setup in a focused ion beam.**

From the additional column, gallium ions are accelerated from a liquid gallium source. The gallium ion beam is focused and scanned with electromagnetic lenses, similar to the electron beam. During ion bombardment of the sample surface, emission of secondary electrons occurs. This makes imaging with ions possible as the electrons can be detected with the standard SEM detectors. As the stopping power is much larger for ions compared to electrons [41] the imaging is more surface sensitive, an advantage used in the helium ion microscope [42]. However, this is not of importance in the FIB, instead the large momentum of the ions is used to sputter the sample atoms off the surface. By selecting preferred areas where the incoming ions should knock out sample atoms, the ions are mainly used for milling.

A common technique to obtain a TEM sample is the lift-out technique as is described by Langford *et al* [43]. The first step is to protect the surface with a fine rectangular strip of platinum. This is done by letting platinum gas into the vacuum chamber with a gas injection system where the gas is cracked on the surface by the ion beam (or, for sensitive samples, by the electron beam). Two trapezoids are then milled on each of the long sides of the rectangle followed by a cleanup until a freestanding sample with an approximate thickness of 800 nm is left. By introduction of a micromanipulator which is welded on the sample with

platinum, the sample can be cut and lifted out with the ion beam. After lift out, the sample is welded on a copper grid dedicated for use in the TEM sample holder. Final thinning and polishing is then performed with decreasing ion currents until electron transparency is achieved.



## CHAPTER 6

---

### *High pressure techniques*

---

To obtain a high pressure, there are in principal two ways to go, either by using a large force or a small area. Techniques for achieving high pressures include the diamond anvil cell (DAC) and the multi anvil press (MA). Both methods are traditionally used in geo-science to simulate earth core conditions. The techniques described in this chapter are the main experiments performed in **Paper II**.

#### **6.1 Diamond anvil cell**

In a DAC, which has been used since the 1950s [44,45], two opposing diamonds are pressing against the sample which is positioned in a hole. The hole, normally a few hundred  $\mu\text{m}$  in diameter, is drilled in a metal gasket, as is seen in the schematic in Figure 9.

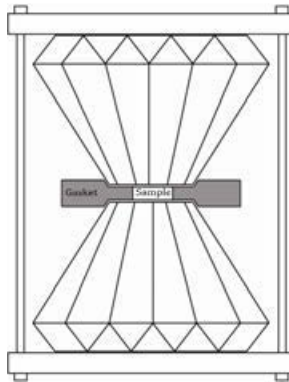


**Figure 9. Schematic picture of a DAC, typical diameter of the hole containing the sample is a few hundred micrometers.**

Thanks to the small dimensions, a pressure of several tens of GPa can be achieved in the cell chamber by adjusting the screws with manual power. Furthermore, as a result of the x-ray transparency of diamonds, the sample characterization can be performed *in situ* if x-rays with high enough intensity are available.

The choice of gasket material is dependent of the desired experimental pressure and temperature ranges, common materials are e.g. stainless steel, tungsten or rhenium. In this work, rhenium was chosen as the most suitable material thanks to its inertness and good properties at the pressures and temperatures used. Prior to drilling the hole, the gasket is pre-indented with the diamonds to a remaining thickness of tens of micrometers. A hole is then drilled with a spark eroder which removes material through an electric discharge.

After completion of drilling the hole, powder grains of the sample is loaded. By additional loading of a pressurizing medium, e.g. NaCl, argon or silicon oil, a nearly hydrostatic pressure is achieved upon compression. The pressurizing medium can also serve as a thermal insulator to protect the diamonds during heating. In the DAC experiments in **Paper II**, NaCl was chosen as a pressurizing medium as it has good thermal properties and because the diffraction peaks do not interfere with those of TiAlN. Grains of ruby are also often loaded in the cell in order to determine the pressure, see section 6.1.2 *Determination of pressure* below.

### 6.1.1 Heating

Heating of the sample is often performed with either laser heating or resistive heating depending on the wanted temperature ranges [46]. Resistive heating is used from room temperature up to 1500 K, where the upper limit is determined by the risk of graphitizing the diamonds. The temperature is easily measured with thermocouples and controlled with a temperature regulator. The whole pressure chamber is heated with small temperature gradients in the sample (<50 °C) and the heating is stable for several hours. A disadvantage with resistive heating is though

that the pressure in the cell is not maintained constant during heating as different parts in the cell have different thermal expansion coefficients.

Laser heating works in a temperature range from around 1000 to above 5000 °C. There are however much larger temperature gradients (>100 °C) and the temperature is often fluctuating. Also, as a thermally insulating medium is used, problems with diffraction might arise as the x-ray reflections from the medium is more intense than those from the sample due to their large volume relative to the sample. Measuring the temperature is also harder to perform compared to electrical heating. This is often carried out with spectroscopic methods together with assumptions of grey body radiation which are uncertain at high pressures and temperatures.

In this work, the diamond anvil cell was used as a complement to the multi anvil press to reach higher temperatures and pressure. Hence, laser heating was used at the maximum temperatures where resistive heating was insufficient.

### 6.1.2 Determination of pressure

The common way of determining the pressure in the cell is by illuminating a ruby grain in the chamber with a laser. By doing this, the ruby is first excited and then emits a light spectrum by fluorescence which is detected. With an increased pressure, the peaks associated to ruby fluorescence are linearly shifted [47] and the obtained pressure can be calculated. This method is often used before and after heating to ensure that no decompression has occurred. Another method is to load a material with a well known equation of state, e.g. gold, in the cell. This enables the possibility to determine the pressure with x-ray crystallography *in situ* during heating.

## 6.2 Multi anvil press

In contrast to the DAC, the MA uses large forces, thereby giving the opportunity to study HPHT behavior for relatively large samples (sample volumes of mm<sup>3</sup> instead of μm<sup>3</sup>). This however makes *in situ* studies and handling of the press more complicated as the dimensions of the whole

setup is much larger. Some stationary MAs though exist at synchrotron beamlines at e.g. APS in Chicago, Spring-8 in Japan and ESRF in France [48]. The sample, usually a powder at first, is often sintered during the experiment due to the high pressures and temperatures used. Hence, due to the limited sample size, the FIB is an excellent instrument for preparing TEM specimens of the sintered samples.

When conducting an experiment, the sample is first enclosed by a cylindrical capsule manufactured of an inert material, e.g. platinum. Dependent of the desired pressure range, the size of the capsule is different where a large capsule gives better statistics but smaller pressures. The capsule is further enclosed by a cylindrical graphite heater and an MgO capsule. The setup is put into an octahedron made of tungsten which is surrounded by eight tungsten anvils. The sample, surrounded by four of the anvils is seen in Figure 10.

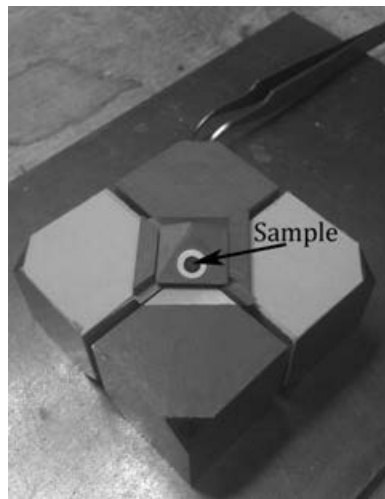


**Figure 10. Multi anvil sample inside an octahedron surrounded by four out of eight tungsten anvils (total size of the shown setup is approximately 10x10 cm).**

The anvil package is then placed in the press which is followed by a hydraulic compression to a desired pressure. Direct measurement and control of the pressure as in the DAC is though not possible, instead the pressure is calibrated with the hydraulic pressure in precedent measurements. A current flows through two corner anvils via the graphite cylinder to generate the needed heat in the cell. The

temperature can be controlled with a thermocouple or by measuring the current together with a calibration table.

In this work, a 1000-ton press has been used together with a platinum cylinder with 1 mm radius and 3 mm height. Typical pressure and temperature ranges for this combination is <20 GPa and <2000 K. The temperatures were controlled with measurements of the current flowing through the graphite oven to minimize any influence from thermocouples.

### **6.3 Sample preparation**

Both the DAC and the MA require a powder, i.e. removing the thin film from its substrate is necessary, which was done chemically in this work. The first step is to grow the thin film on iron sheets which are immersed in hydrochloric acid where the iron is etched away. Prior to this, the backsides of the sheets are mechanically grinded. The grinding has two purposes; removal of the small amounts of coating grown on the backside as well as providing a rough surface for the hydrochloric etching. After removal of all iron, flakes of TiAlN is left which are cleaned in acetone and distilled water for removal of all acid residues. In the final step, the flakes are carefully ground in a mortar together with acetone followed by drying.



# CHAPTER 7

---

## *Metal cutting*

---

The principle behind metal cutting is simple, excessive material is removed until a desired shape is created. To completely understand and explain the underlying procedure is though far from simple and still an unsolved task despite extensive research. This chapter deals with some of the basics occurring during metal cutting. Studies of coatings after metal cutting have been performed in both **Paper I** and **Paper III**.

### **7.1 Temperature distribution**

There are many different methods for studying the temperature distribution [49-53], basically all of them however suffer from uncertainties. In this work, temperature distribution has been measured with an IR-CCD camera using the setup as described in detail by M'Saoubi *et al* [52]. The method was chosen as it has a good resolution and gives the opportunity to extract the temperature profile along the rake face. Selected thermal maps from these measurements are shown in Figure 11. Here, a turning operation in hardened and tempered steel has been performed with  $\text{Ti}_{0.6}\text{Al}_{0.4}\text{N}$  coated on cemented carbide at cutting speeds of 100, 200 and 400 m/min.

An area where the measured cutting temperatures are largest, also called a hot spot, can be seen at all cutting speeds. The position of the hot spot is approximately at half the contact length and is not dependent of cutting speed. The average and maximum temperature is though dependent of the speed as is seen in Figure 11. Extraction of maximum temperatures gives a change from below 800 °C for 100 m/min

to above 950 °C for 400 m/min. One reason for this lies behind the generation of heat which is mainly due to the shearing of the work material and the sliding of the chip [54]. With higher cutting speed, the amount of sheared and sliding work material per time is increasing, thus yielding an increased temperature.

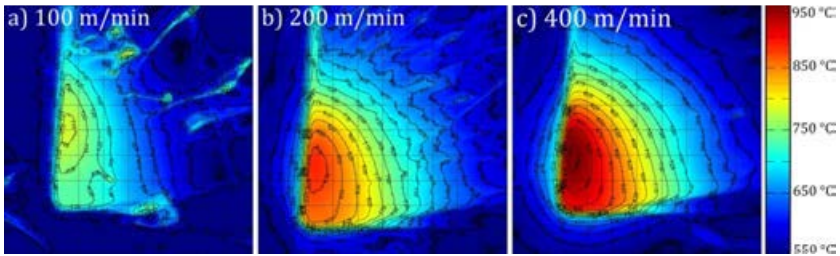


Figure 11. Thermal maps showing the temperature during cutting as measured with an IR-CCD camera at a) 100, b) 200 and c) 400 m/min.

## 7.2 Stress distribution

Determining the stress distribution along the cutting edge is an even more challenging task than determining the temperature distribution. In this work, an analytical model described in detail by Chandrasekaran *et al* [49] was used. The parameters used in the model are the chip thickness, contact lengths, work material shear strength and measured cutting forces. The normal and tangential stress distributions for three different cutting speeds as a function of the contact length are seen in Figure 12.

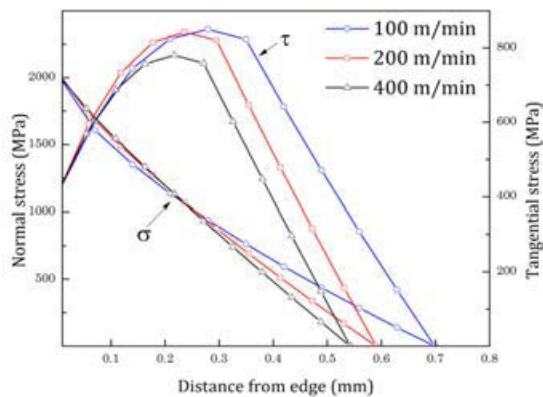
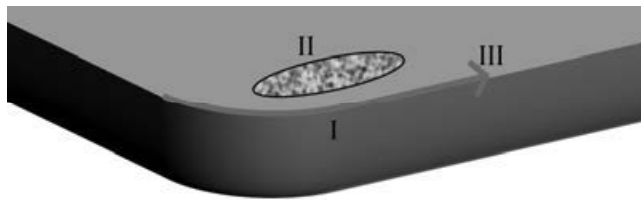


Figure 12. Stress distribution along the rake face at a) 100, b) 200 and c) 400 m/min.

As is seen, the normal stress peaks at the tool tip at values around 2 GPa and is essentially not dependent of the cutting speed. As the distance from the edge increases along the contact length there is an almost linear decrease in normal stress. For the tangential stress, the values are lower and the maximum value occurs around half the contact length. When increasing the cutting speed there is shift towards lower values of the frictional stress. One reason for this might be the substantially higher temperature seen in Figure 11 above which thermally softens the work material.

### 7.3 Wear

The above described thermal and stress distribution is eventually detrimental for the coating properties and despite its high hardness and good adhesion to the substrate, the coating is worn from the substrate. Control, and preferably prediction, of the wear is critical because an uncontrolled wear during a cutting operation may lead to cutting force fluctuations and an impaired surface finish of the tool piece. The most common wear mechanisms are shown in Figure 13 and are crater (I), flank (II) and notch wear (III).



**Figure 13. Schematic picture showing three of the major wear types.**

The sliding chip on the rake face creates a high temperature and a high tangential stress as is seen in Figure 11 and Figure 12 above. At this position, the crater wear (I) commonly begins due to abrasive and chemical wear. A complete breakdown of the cutting edge occurs when the crater reaches the edge of the cutting edge. The monitoring and prediction of the crater wear is difficult which is a disadvantage. In contrast, the flank (II) wear is both predictable and can be monitored by measuring the cutting forces. It is caused by abrasive wear from the

contact with the work material and is one of the reasons behind a poor surface finish of the final work piece. At the depth of cut, in the border zone between the atmosphere and the work material, the notch wear (III) occurs. This wear is most pronounced when cutting in deformation hardening work materials [55].

#### 7.4 Chemical interactions

The high temperature during cutting increases the diffusion rate and the chemical interaction between the coating and its surroundings. At the tool-chip-interface, an adhered layer containing species from the work piece and the atmosphere is often seen during cutting. Figure 14 below shows a STEM micrograph over an adhered layer after metal cutting. The uppermost bright layer is mainly Fe from the work material as determined with an EDS line scan (not shown). More interesting is the layer between the coating and the adhered work material. Corresponding elemental EDS maps show that this first layer primarily consists of Al with small Fe particles. There are small or no traces of Ti in the layer apart from the particle seen in the middle. A possible origin to the appearance of this layer is the out-diffusion of Al from the TiAlN matrix which could also be one of the contributors to the above mentioned crater wear [56,57]. Al diffusion from the work material is though also a possibility.

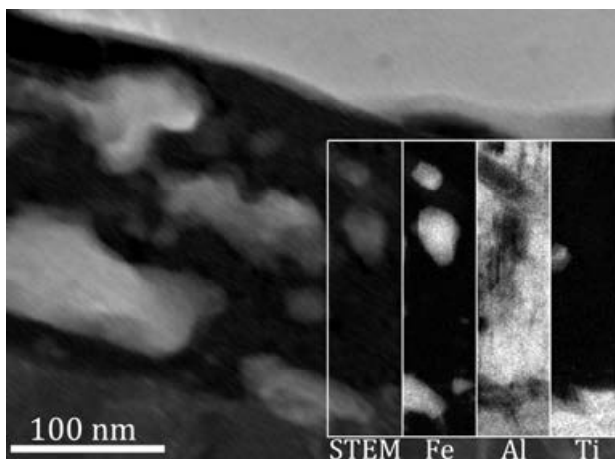
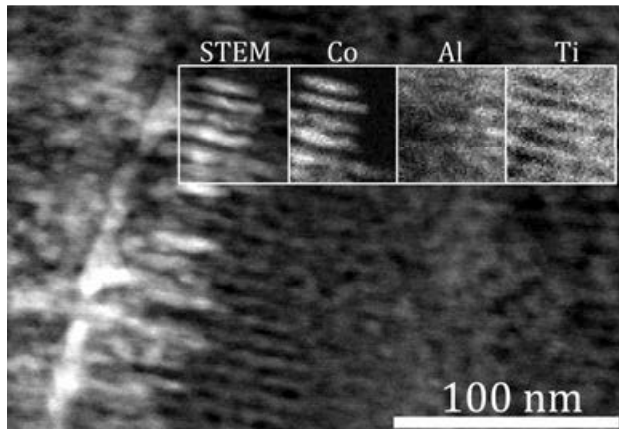


Figure 14. STEM micrograph of the adherent layer with additional elemental EDS maps for Fe, Al and Ti.

Chemical interactions can also take place at the interface between the substrate and the coating. The substrates in this work consist of cemented carbide (WC-Co) and typically Co from the substrate diffuses into the coating. An example of this is seen in the STEM micrograph with corresponding elemental maps in Figure 15 below. From the micrograph it can be seen that Co has diffused through a grain boundary and spread out along the weak layering in the coating stemming from the rotation during deposition. The reason to the out-diffusion in the grain boundary is probably due to their higher diffusivity along the grain boundaries [58]. The chemical interaction between the substrate and the coating can be deteriorates the coating properties and diffusion barriers are often used as an interlayer to prevent such out-diffusion.



**Figure 15. STEM micrograph with EDS elemental maps for Co, Al and Ti showing the diffusion of Co from the substrate into the coating.**



## CHAPTER 8

---

### *Conclusions*

---

The work described in this thesis has shown that the external stress during cutting against the coating promotes a favorable spinodal decomposition of TiAlN. This has been shown through characterizations of worn coatings used in continuous metal cutting where it is seen that the spinodally decomposed domains are larger compared with heat treatments at comparable temperatures. The results hence suggest that the spinodal decomposition reaches its coarsening stage earlier during metal cutting.

Furthermore, it has been shown that the spinodally decomposed domains align along elastically softer directions for anisotropic compositions, which is true after both metal cutting and isothermal heat treatments. This is important as the evolving microstructure during the decomposition is likely to affect the hardness and wear resistance during cutting.

We have also shown, both experimentally and theoretically, that the unwanted transformation of cubic AlN into its hexagonal phase is suppressed with both elevated pressures and temperatures. In addition, the alloying of Ti further enlarges the stability region of cubic AlN. The suppression of this transformation is important as it is detrimental for the coating properties.



---

## *Referenser*

---

- [1] Modern skärande bearbetning: en praktisk handbok, Sandvik Coromant, 1995.
- [2] Metal machining - theory and applications [electronic resource], Arnold, 2000.
- [3] P.H. Mayrhofer, C. Mitterer, L. Hultman, H. Clemens, Progr. in Mater. Sci. 51 (8) (2006) 1032.
- [4] O. Knotek, M. Bohmer, T. Leyendecker, J.Vac. Technol. A 4 (1986) 2695.
- [5] H.A. Jehn, S. Hofmann, V.E. Ruckborn, W.D. Munz, J.Vac. Technol. A 4 (1986) 2701.
- [6] J.C. Knight, Wear 138 (1-2) (1990) 239.
- [7] B. Navinšek, P. Panjan, A. Cvelbar, Surf. Coat. Technol. 74-75 (1995) 155.
- [8] A. Hörling, L. Hultman, M. Odén, J. Sjöln, L. Karlsson, J.Vac. Technol. A 20 (2002) 1815.
- [9] A. Knutsson, M.P. Johansson, L. Karlsson, M. Oden, J. Appl. Phys. 108 (4) (2010)
- [10] A. Knutsson, M.P. Johansson, P.O.Å. Persson, L. Hultman, M. Odén, Appl. Phys. Lett. 93 (14) (2008)
- [11] P.H. Mayrhofer, A. Hörling, L. Karlsson, *et al*, Appl. Phys. Lett. 83 (2003) 2049.
- [12] K.-. Bouzakis, G. Skordaris, S. Gerardis, *et al*, Surf. Coat. Technol. 204 (2009) 1061.
- [13] R. M'Saoubi and S. Ruppi, CIRP Ann. Manuf. Technol. 58 (2009) 57.

- [14] B. Alling, M. Odén, L. Hultman, I.A. Abrikosov, *Appl. Phys. Lett.* 95 (2009)
- [15] D. Holec, F. Rovere, P.H. Mayrhofer, P.B. Barna, *Scr. Mater.* 62 (6) (2010) 349.
- [16] W.D. Callister and D.G. Rethwisch, *Fundamentals of materials science and engineering : an integrated approach*, John Wiley & Sons, 2008.
- [17] D.A. Porter, K.E. Easterling, M.Y. Sherif, *Phase transformations in metals and alloys*, CRC ; Taylor & Francis, 2009.
- [18] ASM handbook. Vol. 8, *Mechanical testing and evaluation*, ASM International, 2000.
- [19] D. Hull and D.J. Bacon, *Introduction to dislocations*, Butterworth Heinemann, 2001.
- [20] [en.wikipedia.org/wiki/File:Strengthening\\_new.svg](http://en.wikipedia.org/wiki/File:Strengthening_new.svg), 2012/03/25
- [21] S. Jonsson, *Mechanical properties of metals and dislocation theory from an engineer's perspective*, Department of Materials Science and Engineering, Royal Institute of Technology, 2007.
- [22] *Handbook of deposition technologies for films and coatings: science, applications and technology*, Elsevier Science, 2010.
- [23] D.M. Mattox, *Met. Finish.* 100 (2002) 394.
- [24] J. Vyskocil and J. Musil, *J. Vac. Sci. Technol. A* 10 (1992) 1740.
- [25] I.G. Brown, *Annu. Rev. Mater. Sci.* 28 (1) (1998) 243.
- [26] F.A. Soliman, O.A. Abu-Zeid, M. Merdan, *Wear* 119 (2) (1987) 199.
- [27] H. Holleck, *Surf. Coat. Technol.* 36 (1-2) (1988) 151.
- [28] A. Hörling, L. Hultman, M. Oden, J. Sjolen, L. Karlsson, *Surf. Coat. Technol.* 191 (2005) 384.
- [29] P.H. Mayrhofer, D. Music, J.M. Schneider, *Appl. Phys. Lett.* 88 (2006)
- [30] F. Tasnádi, I.A. Abrikosov, L. Rogström, J. Almer, M.P. Johansson, M. Odén, *Appl. Phys. Lett.* 97 (2010)
- [31] J.W. Cahn, *Acta Metall.* 10 (3) (1962) 179.
- [32] I. Baker, R.K. Zheng, D.W. Saxey, *et al*, *Intermet* 17 (11) (2009) 886.

- [33] D.E. Winterbone, *Advanced thermodynamics for engineers*, Arnold; Wiley, 1997.
- [34] L. Rogström, J. Ullbrand, J. Almer, L. Hultman, B. Jansson, M. Odén, *Thin Solid Films* (In press) (2012)
- [35] B. Alling, A.V. Ruban, A. Karimi, *et al*, *Phys. Rev. B* 75 (4) (2007)
- [36] F. Peng, D. Chen, H. Fu, X. Cheng, *Phys. B* 403 (23-24) (2008) 4259.
- [37] L. Bayarjargal and B. Winkler, *Appl. Phys. Lett.* 100 (2) (2012)
- [38] W. Feng, S. Cui, H. Hu, W. Zhao, Z. Gong, *Phys. B* 405 (2) (2010) 555.
- [39] A. Siegel, K. Parlinski, U.D. Wdowik, *Phys. Rev. B* 74 (10) (2006)
- [40] D.B. Williams and C.B. Carter, *Transmission Electron Microscopy*, Plenum Press, 1996.
- [41] T. Ishitani, T. Yamanaka, K. Inai, K. Ohya, *Vacuum* 84 (8) (2010) 1018.
- [42] K. Ohya, T. Yamanaka, K. Inai, T. Ishitani, *Nucl. Instrum. Methods. Phys. Res. Sect. B* 267 (4) (2009) 584.
- [43] R.M. Langford and A.K. Petford-Long, *J.Vac. Technol. A* 19 (2001) 2186.
- [44] A.W. Lawson and T.-. Tang, *Rev. Sci. Instrum.* 21 (9) (1950) 815.
- [45] J.C. Jamieson, A.W. Lawson, N.D. Nachtrieb, *Rev. Sci. Instrum.* 30 (11) (1959) 1016.
- [46] L. Dubrovinsky, T. Boffa-Ballaran, K. Glazyrin, *et al*, *High. Press. Res.* 30 (4) (2010) 620.
- [47] J.D. Barnett, S. Block, G.J. Piermarini, *Rev. Sci. Instrum.* 44 (1) (1973) 1.
- [48] R.C. Liebermann, *High. Press. Res.* 31 (4) (2011) 493.
- [49] H. Chandrasekaran and A. Thuvander, *Mach. Sci. Technol.* 2 (1998) 355.
- [50] M.A. Davies, T. Ueda, R. M'Saoubi, B. Mullany, A.L. Cooke, *CIRP Ann. Manuf. Technol.* 56 (2007) 581.
- [51] R. M'Saoubi and H. Chandrasekaran, *Int. J. Adv. Manuf. Technol.* 56 (2011) 865.

[52] R. M'Saoubi and H. Chandrasekaran, *Int. J. Mach. Tools Manuf.* 44 (2004) 213.

[53] R. M'Saoubi, C. Le Calvez, B. Changeux, J.L. Lebrun, *Proc. Inst. Mech. Eng. Pt. B: J. Eng. Manuf.* 216 (2002) 153.

[54] A. Liljerehn, V. Kalhori, M. Lundblad, *Mach. Sci. Technol.* 13 (4) (2009) 488.

[55] J.P. Davim, *Machining of Hard Materials* [electronic resource], Springer-Verlag London, 2011.

[56] H.O. Gekonde and S.V. Subramanian, *Surf. Coat. Technol.* 149 (2-3) (2002) 151.

[57] A. Molinari and M. Nouari, *Wear* 252 (1-2) (2002) 135.

[58] P.P. Chattopadhyay, S.K. Pabi, I. Manna, *Mater. Chem. Phys.* 68 (1-3) (2001) 80.

---

## *Summary of included papers*

---

### **8.1 Paper I**

In this paper,  $\text{Ti}_{0.6}\text{Al}_{0.4}\text{N}$  was deposited on tungsten carbide substrates. This was followed by a longitudinal cutting operation in steel with a cutting speed of 200 m/min, feed of 0.3 mm/revolution, a 3 mm depth of cutting and a time in cut of 10 min. Metal cutting was also performed while measuring forces and temperature. Additionally, heat treatments with a 10 min isothermal step of 900 °C and 1000 °C respectively were performed for comparison. The *ex-situ* characterization was mainly performed with STEM.

The results show a peak temperature below 900 °C and a peak normal stress of 2 GPa during cutting. The size of the decomposed domains after metal cutting are measured and compared with heat treated samples. It can from these measurements be concluded that the spinodal decomposition is not only affected by the temperature distribution but is also promoted by the external stress acting on the cutting insert.

### **8.2 Paper II**

This paper studies the high HPHT behavior of  $\text{Ti}_{0.6}\text{Al}_{0.4}\text{N}$  by using multi anvil press and diamond anvil cell techniques. Cathodic arc evaporated TiAlN was deposited onto steel substrates which were dissolved in hydrochloric acid, thus providing the coating in powder form after grinding. Temperatures and pressures up to 2200 °C and 23 GPa

respectively were obtained using a combination of the above mentioned instruments. *Ex-situ* characterization was performed using a combination of XRD and TEM. Additionally, a (P,T) phase diagram of pure AlN showing the equilibrium line between c-AlN and h-AlN were calculated using first principles calculations.

Results of the first principle calculations show an increased stability of c-AlN with both an increased pressure and temperature. XRD results of TiAlN further strengthens the first principle calculations as an increasing temperature at isotherms as well as an increased pressure at isobars stabilizes c-AlN. It is also concluded, by comparing the experimental values of TiAlN with the theoretical of AlN, that the adding of Ti into AlN further stabilizes c-AlN. The reason for this might be the template effect as AlN-rich domains are surrounded by cubic regions of TiN-rich domains in combination with the energy that would be added to the system by the highly strained h-AlN.

### **8.3 Paper III**

The focus of this paper is the effect of anisotropy on the spinodal decomposition after heat treatments as well as after metal cutting. Both  $\text{Ti}_{0.6}\text{Al}_{0.4}\text{N}$  and  $\text{Ti}_{0.33}\text{Al}_{0.67}\text{N}$  have been investigated, where the former is close to the isotropic limit and the latter is highly anisotropic. The coatings have been characterized with analytical TEM at high symmetry zone axes. The results show that the spinodally decomposed domains have a tendency to align along elastic compliant  $\langle 100 \rangle$  directions in the anisotropic coating as these are elastically softer. For the  $\text{Ti}_{0.6}\text{Al}_{0.4}\text{N}$ , which has a more isotropic behavior, the decomposed domains are instead rounder and distributed in random direction.